

A 3D acoustic propagation model for shallow waters based on an indirect Boundary Element Method

E. F. Lavia, J. D. Gonzalez & S. Blanc

March 17, 2022

Abstract

The purpose of this work is twofold: (a) To present the theoretical formulation of a 3D acoustic propagation model based on a Boundary Element Method (BEM), which uses a half-space Green function in place of the more conventional free-space Green function and (b) to show a numerical implementation aimed to explore the formulation in simple idealized cases –controlled by a few parameters–, and provides necessary tests for the accuracy and performance of the model. The half-space Green’s function, which has been used previously in scattering and diffraction, adds terms to the usual expressions of the integral operators without altering their continuity properties. Verifications against the Pekeris waveguide suggest that the model allows an adequately prediction for the acoustic field. Likewise, numerical explorations in relation to the necessary mesh size for the description of the water-sediment interface allow us to conclude that a TL prediction with acceptable accuracy can be obtained with the use of a bounded mesh around the desired evaluation region.

1 Introduction

Underwater sound propagation is significantly affected by three-dimensional (3D) effects due to the complex realistic ocean environment. The importance of these effects has been early recognised [1, 2] and even emphasized by at-sea and/or at-laboratory measurements [3].

A great variety of models have been developed to estimate underwater sound propagation in 3D scenarios that, according to their governing equations and numerical approaches, can be categorized into three main groups [4], namely, (a) extended parabolic equation (PE) models, such as the efficient marching solution based on the parabolic equation proposed by [12] that is applied to a local and to a global ocean environment by [6] and [5], respectively; (b) normal mode models [7, 8, 9]; and (c) ray and beam tracing models [10, 11]. However, modelling acoustic propagation for 3D environments is still a significant two-fold challenge due to both the difficulties associated with a thorough comprehension of the physical phenomenon and the high computational time costs.

On the other hand, methods based on boundary integration, particularly the Boundary Element Method (BEM), have been applied to a stratified oceanic media in shallow waters. Although the BEM is computationally expensive than other methods, acceleration algorithms can be used to improve its performance but it is still not capable to model realistic scenarios for long-range propagation (several thousand of kilometres). Nevertheless, the method still has its strong advantages such as a clean mathematical formulation and a consistent behaviour at infinity (where the fields are expected to vanish).

The BEM consists on defining the acoustic field through surface-integral operators reducing the definition of the computational domain from 3D to 2D. Several references can be found in the literature, as [17] who used a multi-layer approach for shallow waters by defining boundary integral equations whose unknowns are the pressure field and the normal particle velocity on the surfaces; this approach can be categorized as a direct BEM approach.

The continuous growth in computational power (hardware equipped with more raw processing power and more memory capacity) opens up the game for methods based on volume or boundary discretization as the Finite Element Method (FEM) and the Boundary Element Method (BEM) (these examples are not exhaustive). These methods allow for a more realistic modelling since they assume fewer hypotheses than classical and well established ones as the ray methods, parabolic equation methods and coupled normal modes [13], which have been successfully used for several decades. The above mentioned assumptions generally refer to symmetry conditions or their validity in certain frequency regimes.

In this work we present a numerical implementation of BEM capable of tackling the acoustic propagation problem in a homogeneous medium with an arbitrary bathymetry (range-dependent model) that can be easily extended to a multilayer coupled approach to consider inhomogeneous media. This formulation includes an appropriate half-space Green function in order to take into account an infinite pressure release surface which is a representation of the ocean free surface in an exact analytical way. This idea has already been used in [14] for a BIEM (Boundary Integral Equation Methods) solution for the acoustic scattering from the surface of a waveguide then applied to a two-dimensional case with non-penetrable boundaries, in [15], and in [16] within the context of acoustic scattering and radiation. The approach presented here uses a modified green function in order to avoid generating a mesh corresponding to the interface ocean-atmosphere. The indirect BEM leads to operators that are numerically well-behaved in comparison with the direct methods such as [17] that needs some preconditioners to numerically solve the problem.

This paper is organized as follows. In Section 2 the BEM model is presented. The boundary value problem corresponding to acoustic propagation in a waveguide is stated in Section 2.1, then the BEM theoretical formulation based on a half-space Green function –emphasizing the differences with those based on the free-space function– is developed in Section 2.2, and finally an outline of the numerical method is provided in Section 2.3. Certain more technical mathematical aspects and some intermediate steps in the derivations are confined to the appendices. In Section 3 numerical experiments aimed to verify the BEM model are carried out. To this end a wave-number integration technique applied to the propagation problem of a Pekeris waveguide provided with a sediment layer (with and without attenuation) is used as a benchmark. Section 4 shows the performance of the model in a shallow water waveguide with a conical mountain, which provides as a range-dependent bathymetry. The conclusions of the work and suitable further steps aimed to improve the model are summarized in Section 5.

2 Model Formulation

2.1 Acoustic propagation problem

The problem of the underwater sound propagation in a homogeneous waveguide with range dependent bathymetry is schematically shown in Figure 1. A time harmonic point source of circular frequency ω is located in an homogeneous water layer (which defines the volumetric region R_0) bounded above by the plane surface Γ_0 and below by the arbitrary surface Γ_1 . The latter limits an unbounded volumetric region R_1 that constitutes a marine sediment layer. The surfaces Γ_0, Γ_1 represent the interfaces seawater-atmosphere and seawater-marine sediments, respectively. Each region R_i ($i = 0, 1$) is characterized by constant acoustic properties c_i, ρ_i (sound speed and density) and wavenumber $k_i = \omega/c_i$. The boundless nature of the R_1 region is emphasized in the scheme by the dashed line at the bottom.

The given point source generates, through interaction with the boundaries, acoustic pressure fields p_i in each region R_i that are solutions of the scalar Helmholtz equation

$$(\nabla^2 + k_i^2) p_i = 0. \quad (1)$$

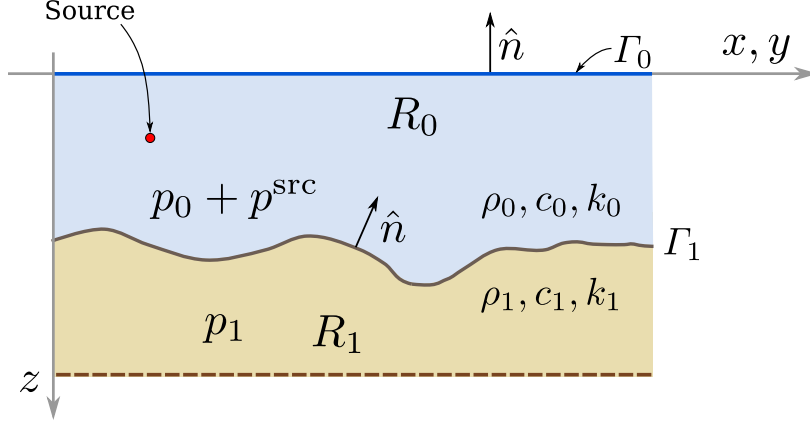


Figure 1: Scheme for the propagation problem. It should be noted that neither cylindrical nor plane symmetry must be inferred from this 2D sketch.

If the source field is p^{src} , then the total field in the region R_0 is $p = p_0 + p^{\text{src}}$. As it is usual in propagation problems, the boundary condition at Γ_0 assumes a pressure-release surface (Dirichlet) ($p_0 + p^{\text{src}} = 0$), whereas at Γ_1 the pressure field must satisfy the transmission condition that arises from demanding continuity of both, the field and the normal particle velocity $v_n = -1/(i\omega\rho)\partial_n p$ (the notation ∂_n is a common abbreviation for the normal derivative $\hat{n} \cdot \nabla$). The point source located at x_{src} is assumed to generate a field

$$p^{\text{src}}(x) = \frac{e^{ik_0|x-x_{\text{src}}|}}{|x-x_{\text{src}}|},$$

with unitary amplitude.

According to the mathematical framework appropriate to BEM (integral operators theory), it is convenient [22] to transform the fields according to

$$u_0 = \frac{p_0}{\rho_0}, \quad u_1 = \frac{p_1}{\rho_1}, \quad u^{\text{src}} = \frac{p^{\text{src}}}{\rho_0}, \quad (2)$$

which has the consequence of making the factors ρ_i^{-1} drop out from the normal derivatives. In terms of these fields u_i the pressure release condition at Γ_0 leads to

$$u_0(x) + u^{\text{src}}(x) = 0 \quad \text{for } x \in \Gamma_0, \quad (3)$$

whereas the requirement of continuity in the field and its derivative at Γ_1 (i.e. the boundary conditions at the interface) implies

$$\left. \begin{aligned} \rho_0 u_0(x) - \rho_1 u_1(x) &= -\rho_0 u^{\text{src}}(x) \\ \partial_n u_0(x) - \partial_n u_1(x) &= -\partial_n u^{\text{src}}(x) \end{aligned} \right\} \text{ for } x \in \Gamma_1 \quad (4)$$

The differential equations given in Eq. (1) and the conditions of Eqs. (3) and (4) constitute the boundary value problem that models the acoustic propagation problem schematized in Figure 1. In the next section this problem will be posed under a mathematical formulation appropriate for an indirect boundary element method BEM.

2.2 BEM formulation with a half-space Green function

A typical indirect BEM formulation for the acoustic propagation problem previously introduced presupposes that each field u_i is expressed as a linear combination of certain kind of surface integrals

as, for example, in

$$u_i(x) = a \int_{\Gamma} \Phi(x, y) \varphi(y) dS_y + b \int_{\Gamma} \partial_{n_y} \Phi(x, y) \sigma(y) dS_y, \quad (5)$$

where the *kernel* function $\Phi(x, y)$ and its normal derivative are two-point functions which give the field x -dependence while the integration (over the boundary Γ) is carried out in the y -variable, the latter emphasized by the sub-index in the surface differential dS_y . Coefficients a, b are known constants while φ, σ are functions to be determined. Each integral in Eq. (5) can be interpreted as an *integral operator* [Ref] acting on a function, for which the usual nomenclature is

$$U[\varphi](x) = \int_{\Gamma} \Phi(x, y) \varphi(y) dS_y, \quad (6)$$

where U represents the operator (associated with a kernel Φ), and φ the function which is integrated on the surface Γ . As will be seen later, the field-values $\varphi(y)$ on Γ will be unknown quantities for the integral formulation of our boundary value problem for acoustic propagation.

In the vast majority of 3D BEM applications associated to the Helmholtz equation, the kernel function $\Phi(x, y)$ is the free-space Green function in the wavenumber k_i ,

$$G(k_i; x, y) = \frac{e^{ik_i|x-y|}}{4\pi|x-y|}, \quad (7)$$

which has the property of being a solution of the Helmholtz equation in absence of boundaries (that is the reason why it is dubbed *free-space*). It should be noted that if the kernel satisfies the Helmholtz equation (where the Laplacian is taken with regard to the x -variable) then its associated operator also does it, as long as the interchange between the integral sign and the laplacian is possible. This kernel $G(k_i; x, y)$ and its normal derivative define the operators

$$S_i[\varphi](x) = \int_{\Gamma} G(k_i; x, y) \varphi(y) dS_y, \quad K_i[\varphi](x) = \int_{\Gamma} \partial_{n_y} G(k_i; x, y) \varphi(y) dS_y,$$

in which the sub-index associates the operator with the wavenumber k_i or equivalently with the R_i region. These S_i, K_i operators constitute the basis for all BEM methods and are called the single layer potential operator (SLP) and the double layer potential operator (DLP), respectively. Since the spherical symmetry of $G(k_i; x, y)$ offers no special advantages for the propagation problem under consideration (because the boundaries are not spherical), a typical BEM formulation would involve integration in both Γ_0 and Γ_1 , i.e. it would require numerical discretization of both these boundaries.

It is also worth noting that although the water and sediment layers are schematized in Figure 1 without borderlines, the x, y directions, in the underwater acoustic propagation modelling it is assumed that these limits are far away from the area of interest so their effects can be neglected. In fact, this assumption implies that the solution for a limited area near the source is identical to a solution for an acoustic problem which has those limits located at infinity. By using this feature it is possible to use a modified Green function which takes into account part of the boundaries of the problem in an exact way, avoiding thus the need of building a discretized version of those boundaries and consequently also avoiding to integrate over them.

Beyond the free-space Green function, the simplest useful modification is the half-space Green function, obtained by using the *image method* [18] which is of widespread application in acoustics and optics (the Rayleigh-Sommerfeld correction to the problem of diffraction by an aperture being an iconic example). The half-space Green function appropriate to our problem will be the solution of the Helmholtz equation valid for a semi-space $z > 0$ where the (infinite) boundary plane $z = 0$ is such that over it the Green's function becomes zero. Its expression is

$$\overline{G}(k_i, x, y) = G(k_i; x, y) - \frac{e^{ik_i|x-y'|}}{4\pi|x-y'|}, \quad (8)$$

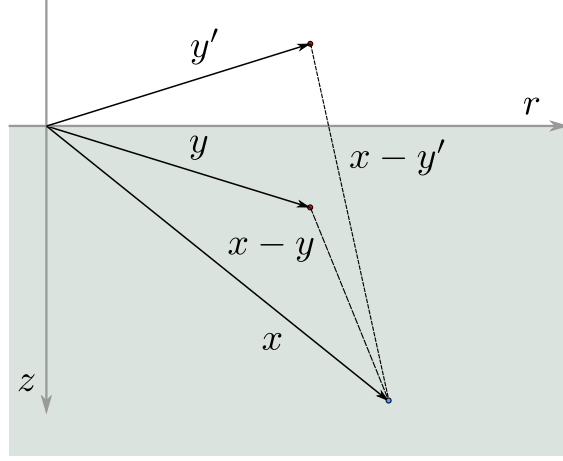


Figure 2: Points and vectors associated to the half-space Green function. For point x, y appearing in the argument of the usual Green function, the half-space variant considers a point y' , specular reflection of y by the $z = 0$ plane.

where y' is the specular image of the point y by the plane $z = 0$. The Figure 2 shows the points x, y, y' involved in the definition of \bar{G} . It is important to emphasize that the modification in Eq. (8) (an extra term) can be interpreted as a new source, an image source, located at point y' outside of the physical region where the acoustic problem is being solved.

Regarding the propagation problem depicted in the Figure 1, the use of a half-space Green function as kernel in the S, K operators implies that the propagation problem satisfies a pressure-release surface condition *built-in*, in the sense that u_0 from (5) is equal to zero over Γ_0 . However, as it is stated in the condition (3), it is desirable a little more on Γ_0 , namely $u_0 + u^{\text{src}} = 0$, one way for that to happen is by redefining u_0 as $u_0 - u^{\text{src}}$, where u^{src} is the image source

$$u^{\text{src}'}(x) = \frac{1}{\rho_0} \frac{e^{ik_0|x-x_{\text{src}'}|}}{|x-x_{\text{src}'}|}.$$

The problem solution in terms of these operators, plus the subtraction of the image source, automatically will take into account the surface Γ_0 so that an explicit evaluation of the boundary conditions there is not necessary. The fields u_i have now to fulfill boundary conditions only at Γ_1 .

Furthermore, writing the solution through the half-space Green function implies that the solution of the propagation problem without the existence of Γ_1 (or with Γ_1 located at infinity) is (or tends to) the image solution

$$\bar{u}^{\text{src}} = u^{\text{src}} - u^{\text{src}'}, \quad (9)$$

2.2.1 BEM formulation

Now, after having chosen an appropriate kernel function, the fields u in each region R will have the following integral representation

$$\begin{aligned} u_0(x) &= S_0[\phi](x) + K_0[\psi](x) - u^{\text{src}'}(x) & \text{for } x \in R_0 \\ u_1(x) &= S_1[\phi](x) + K_1[\psi](x) & \text{for } x \in R_1 \end{aligned} \quad (10)$$

where

$$S_i[\phi](x) = \int_{\Gamma_1} \bar{G}(k_i; x, y) \phi(y) dS_y \quad K_i[\psi](x) = \int_{\Gamma_1} \partial_{n_y} \bar{G}(k_i; x, y) \psi(y) dS_y$$

are the SLP and the DLP operators, evaluated on the unknown functions ϕ and ψ , respectively. Since the boundary conditions of Eq. (4) involves the normal velocity it will be necessary to evaluate normal derivatives of these operators. This procedure leads to two new operators,

$$K'_i[\phi](x) = \partial_{n_x} \left(\int_{\Gamma_1} \bar{G}(k_i; x, y) \phi(y) dS_y \right) \quad T_i[\psi](x) = \partial_{n_x} \left(\int_{\Gamma_1} \partial_{n_y} \bar{G}(k_i; x, y) \psi(y) dS_y \right),$$

generically known as the *normal derivative operators* [21].

The next step in the integral formulation is to evaluate the transmission conditions at Γ_1 , Eq. (4), using the field prescription according to (10). This process requires to carefully consider the operator's *jump conditions* (section 3.1 of reference [24]) or, in other words, its behavior in the limit when its evaluation point x in the surface is approached from R_i along the normal vector direction n_x . Following these steps the following system of two boundary integral equations

$$\left. \begin{aligned} (\rho_0 K_0 - \rho_1 K_1 + 1/2 \alpha_{01})[\psi](x) + (\rho_0 S_0 - \rho_1 S_1)[\phi](x) &= -\bar{u}^{\text{src}}(x) \\ -\mathcal{M}_{01}[\psi](x) + (I - \rho_0 K'_0 + \rho_1 K'_1)[\phi](x) &= \partial_n \bar{u}^{\text{src}}(x) \end{aligned} \right\} \text{ for } x \in \Gamma_1 \quad (11)$$

for the two unknowns ϕ, ψ is obtained, where $\alpha_{01} = (\rho_0 + \rho_1)/2$ and \mathcal{M} is another operator, called the Müller operator and defined as

$$\mathcal{M}_{s\ell}[\varphi](x) \equiv T_s[\varphi](x) - T_\ell[\varphi](x). \quad (12)$$

The Appendix A provides a schematic derivation of the system of Eq. (11) by evaluating carefully the limits and using the jump conditions from [24].

The modification in \bar{G} with respect to the usual G , i.e. the addition of an image source at y' , modifies the usual expression for the integrands in the operators S, K, K', T . Nevertheless, these modifications does not alter its continuity and jump properties because the added term in \bar{G} is regular for all x, y in the physical domain. In the Appendix B expressions for all the four integral operator's integrands are provided.

The solution of the acoustic propagation problem given in terms of the fields u_i has been transformed in the search of the functions ψ, ϕ both having the surface Γ_1 as their domains of definition. These functions are called *densities* in the literature and are now the unknowns. The BEM method provides a procedure to find discretized versions of these densities, which will be the subject of the next section.

2.3 Numerical method

The system of Eq. (11) can be solved through a discretization process over the boundary Γ_1 , which turns it in a finite-size matrix system. For this step the standard procedure is to assume the following two approximations.

1. The surface Γ_1 is approximated by a planar triangular mesh (i.e., a set of N_1 triangles $\{\Delta_\ell\}$ with $\ell = 1, 2, \dots, N_1$), so that

$$\Gamma_1 = \bigcup_{\ell=1}^{N_1} \Delta_\ell,$$

where Δ_ℓ is the ℓ -th triangle whose centroid is x_ℓ .

2. The unknown densities ψ and ϕ are considered as piecewise constant functions in each triangle, that is,

$$\psi(x) = \sum_{\ell=1}^{N_1} \psi_\ell I_{\Delta_\ell}(x) \quad \phi(x) = \sum_{\ell=1}^{N_1} \phi_\ell I_{\Delta_\ell}(x), \quad (13)$$

where $\psi_\ell \equiv \psi(x_\ell)$, $\phi_\ell \equiv \phi(x_\ell)$ are unknown complex numbers and $I_{\Delta_\ell}(x)$ is the indicator function of the ℓ -th triangle, defined as

$$I_{\Delta_\ell}(x) = \begin{cases} 1 & \text{if } x \in \Delta_\ell \\ 0 & \text{otherwise} \end{cases}$$

In order to find the densities, the prescriptions (13) are inserted in the system (11). This procedure transforms each integral over the boundary Γ_1 into a sum of integrals over each triangle Δ_ℓ .

The resulting system remains, of course, valid for all $x \in \Gamma_1$, so that is valid in particular for the set of centroids $\{x_\ell\}(\ell = 1, 2, \dots, N_1)$ of the triangles belonging to Γ_1 . When these discretized equations are evaluated in the set $\{x_\ell\}$, a matrix system of size $2N_1 \times 2N_1$

$$(\mathbf{B} + \mathbf{D}) \begin{pmatrix} \boldsymbol{\psi} \\ \boldsymbol{\phi} \end{pmatrix} = \begin{pmatrix} \mathbf{f} \\ \mathbf{g} \end{pmatrix} \quad (14)$$

is obtained. The complex-valued vectors $\boldsymbol{\psi}, \boldsymbol{\phi}$ containing the unknowns and the data vectors \mathbf{f} and \mathbf{g} are defined as

$$\boldsymbol{\psi} = \begin{pmatrix} \psi_1 \\ \psi_2 \\ \vdots \\ \psi_{N_1} \end{pmatrix} \quad \boldsymbol{\phi} = \begin{pmatrix} \phi_1 \\ \phi_2 \\ \vdots \\ \phi_{N_1} \end{pmatrix} \quad \mathbf{f} = - \begin{pmatrix} -\rho_0 \bar{u}^{\text{src}}(x_1) \\ -\rho_0 \bar{u}^{\text{src}}(x_2) \\ \vdots \\ -\rho_0 \bar{u}^{\text{src}}(x_{N_1}) \end{pmatrix} \quad \mathbf{g} = \begin{pmatrix} \partial_n \bar{u}^{\text{src}}(x_1) \\ \partial_n \bar{u}^{\text{src}}(x_2) \\ \vdots \\ \partial_n \bar{u}^{\text{src}}(x_{N_1}) \end{pmatrix}. \quad (15)$$

The complex-valued matrices \mathbf{B} and \mathbf{D} are defined as 2 block-matrix, each block having size $N \times N$

$$\mathbf{B} = \begin{bmatrix} (\rho_0 \mathbf{K}_0 - \rho_1 \mathbf{K}_1) & (\rho_0 \mathbf{S}_0 - \rho_1 \mathbf{S}_1) \\ -\mathcal{M}_{01} & (\mathbf{K}'_1 - \mathbf{K}'_0) \end{bmatrix}, \quad \mathbf{D} = \begin{bmatrix} 1/2 \alpha_{01} \mathbf{I} & \mathbf{0} \\ \mathbf{0} & \mathbf{I} \end{bmatrix} \quad (16)$$

where \mathbf{I} is the identity matrix of dimension N_1 . The boldface typography used for the operator's matrix representation attempts to capture its discrete nature. For a generic operator $\mathbf{U}_q \in \mathbb{C}^{N_1 \times N_1}$ with kernel $\Phi(k_q; x, y)$ the i, j matrix element represents

$$[\mathbf{U}_q]_{ij} = \int_{\Delta_j} \Phi(k_q; x_i, y) dS_y.$$

The matrix row-index i is associated with a particular evaluation point x_i while the column index j is associated with the particular element Δ_j . The subindex q identifies the corresponding wavenumber k_q . For example,

$$[\mathbf{S}_1]_{\ell s} = \int_{\Delta_s} \bar{G}_{k_1}(x_\ell, y) dS_y,$$

implies integration over the s -th triangle of Γ_1 and evaluation on centroid x_ℓ , all for the wavenumber k_1 .

Numerical evaluation of the operators can be cumbersome since it involves the resolution of integral singularities. In this case, computer implementation is strongly based on the previous work of [20] that uses the traditional free-space Green function as integral kernel. Thus, the numerical evaluation of the matrix components at Eq. (16) is carried out by taking that previous implementation and changing the Green function. Even though this process is long and implies many calculations, this is straightforward, because, as was it previously stated, the kernel is modified by adding a term that is regular for all x, y in the physical domain, meaning that there is no need to develop additional numerical treatments of singularities.

Once the matrix system of Eqs. (14), (15) and (16) is solved and density vectors $\boldsymbol{\phi}, \boldsymbol{\psi}$ are obtained, we are ready to evaluate the field in any point x belonging to the physical domain.

2.4 Pressure and TL computation

After having chosen the densities ψ, ϕ , the fields u_i (in water or in the sediment layer) can be calculated by evaluating the corresponding integral representation in Eq. (10) with the piecewise approximation made at Eq. (13). Therefore, using the transformation (2) the discretized version of the pressure field in the water layer is

$$p_0(x) = -u^{\text{src}'}(x) + \sum_{\ell=1}^{N_1} \left(\rho_0 \phi_\ell \int_{\Delta_\ell} \bar{G}(k_0; x, y) dS_y + \rho_0 \psi_\ell \int_{\Delta_\ell} \partial_{n_y} \bar{G}(k_0; x, y) dS_y \right). \quad (17)$$

As it is common in acoustic propagation modelling, in the following sections results for acoustic propagation evaluation will be analyzed in the logarithmic scale using the transmission loss (TL) parameter which is defined as

$$\text{TL} = -20 \log_{10} \left(\left| \frac{p_0(x)}{p_{\text{ref}}} \right| \right) \quad \text{dB re 1 m}, \quad (18)$$

where the reference pressure p_{ref} is the pressure evaluated at 1 m from the source.

3 Model verifications: Pekeris waveguide

In order to verify the BEM model the classical problem of propagation in a Pekeris waveguide was used as a benchmark solution. It consists of a flat homogeneous water layer bounded below by a homogeneous half-space of higher sound speed and above by a pressure-release interface. Such a setup, first analyzed within normal mode theory [23], is a simple but useful model for acoustic propagation in shallow-water ocean environments. This configuration is one of the most employed benchmark solutions because it allows an analytical treatment by using wavenumber integration techniques and it is intrinsically important due to the physical insight that it provides. In the next subsection an overview of the exact solution and a benchmark case used for verification is presented. Next, comparisons between BEM model and the exact solution are also included.

3.1 Pekeris waveguide solution

The Pekeris waveguide considered as our benchmark setup is shown in Figure 3. A homogeneous water column of depth D , sound speed c_0 and density ρ_0 overlies an homogeneous fluid half-space of sound speed c_1 and density ρ_1 . A point source located in water at $(r, z) = (0, z_s)$ generates a pressure field

$$p(r, z) = -\rho_0 \omega^2 S_\omega \frac{e^{ik_0|(r,z)-z_s|}}{4\pi|(r, z) - z_s|},$$

where S_ω is the source strength. The physical parameters c, ρ and location z_s of source and receiver depth z used in this example were taken from an example in [18] and are explicitly indicated in the figure.

The pressure $p(r, z)$ in the Pekeris waveguide is then given by

$$p(r, z) = \begin{cases} \rho_0 \omega^2 \psi_0(r, z), & 0 \leq z \leq D \\ \rho_1 \omega^2 \psi_1(r, z), & z \geq D \end{cases}$$

where the ψ_i ($i = 0, 1$ corresponding to the water and sediments layers, respectively) are the displacement potentials which can be expressed as Hankel transforms

$$\psi_i(r, z) = \int_0^\infty \Psi_i(k_r, z) J_0(k_r r) k_r dk_r,$$

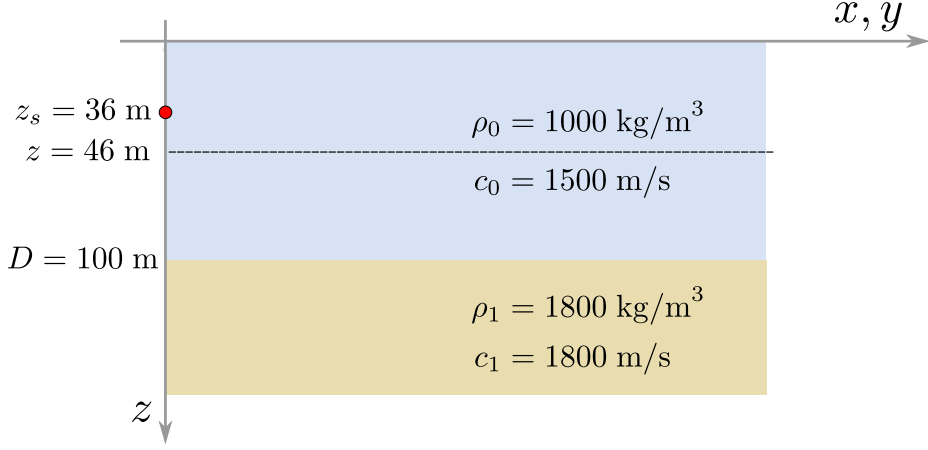


Figure 3: Pekeris waveguide of thickness $D = 100$ m with pressure-release surface and penetrable bottom. The physical parameters ρ, c in each layer are indicated in the figure.

being J_0 the cylindrical Bessel function of first kind and $\Psi_i(k_r, z)$ the solution of the depth-dependent wave equation

$$\left(\frac{d^2}{dz^2} + k_{z,i}^2 \right) \Psi_i(k_r, z) = \frac{S_\omega}{2\pi} \delta(z - z_s),$$

where $k_{z,i}^2 = k_i^2 - k_r^2$ is the vertical wavenumber in the i -medium. Attenuation in the sediment layer is taken into account through a complex wavenumber $K = k_1 (1 + i \eta \alpha)$, where the coefficient α quantifies its strength and $\eta = 1/(40 \pi \log_{10} e)$ is a numeric constant that turns dimensionless the imaginary part. Usually, attenuation α is given in dB/wavelength. Further details and physical analysis of this solution can be founded in [18].

3.2 BEM model applied to the Pekeris waveguide

The BEM model was compared to the Pekeris benchmark solution previously presented at frequency $f = 5$ Hz by evaluating transmission loss (TL) (a) along a 2500 m path at $z = 46$ m depth (inside the water layer, see Figure 3) and (b) in a rectangle 2500 m width and 150 m depth which encompass both water and sediment field evaluations. Two cases are considered; without attenuation and with an attenuation $\alpha = 5$ dB/ λ (from the applications standpoint is a somewhat big value, its inclusion being justified only to test the model in a broad spectrum of its parameters). All the simulations were conducted over a circular mesh of radius $R = 2500$ m and $N = 49009$ triangles which represents the boundless interface water-sediments.

Since our BEM formulation assumes constant field on each triangle, the number N of elements of the mesh must be chosen to ensure that the acoustic wavelength would be several times greater than the distance between vertices (usually five or six times greater) according to the usual practice in scattering applications [19]. In the circular mesh used for this verification test, the previous requirement is fulfilled by the 96 % of the triangle's sides.

The results of the comparison are shown in Figure 4, where the top panel shows the case without attenuation ($\alpha = 0$) and the bottom one the case with an strong attenuation $\alpha = 5$ dB/ λ . The evaluation coordinate r reaches the very end of the mesh so that errors are expected there. They are evident in the case $\alpha \neq 0$ but almost unnoticeable in the $\alpha = 0$ dB/ λ case. The former assumption about the pseudo-local character of the fields, i.e. the fact that the field at very long distances is not needed to determine the field in a restricted domain, appears to be a valid one. Of course, in cases where a benchmark solution is not available, which portions of the domain need to be meshed it should be object of analysis.

The Figures 5 and 6 show the transmission losses for a rectangle which encompasses water and

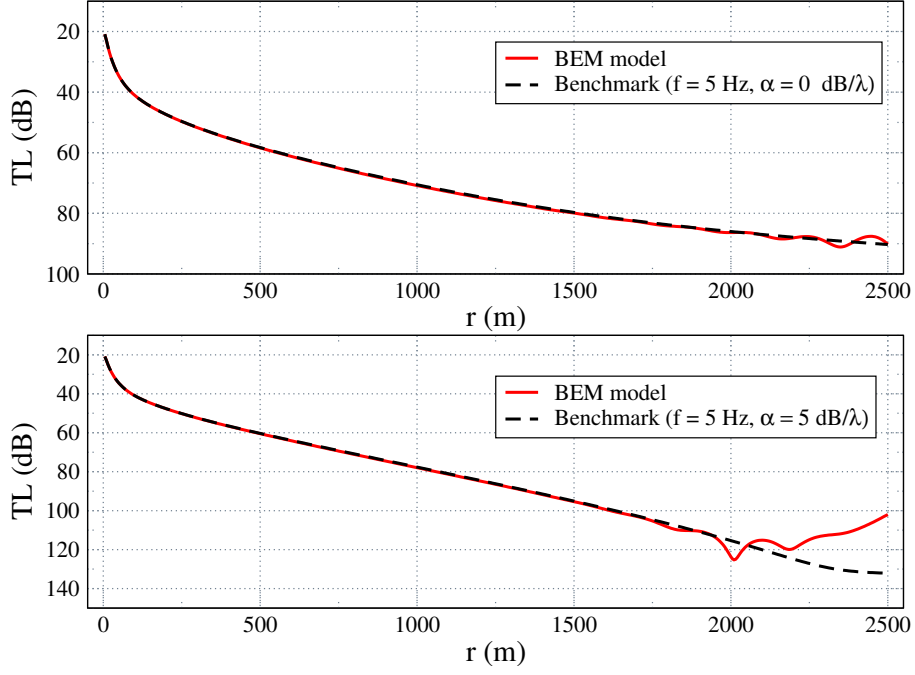


Figure 4: Transmission loss (TL) vs. range computed by the BEM model (full lines) and by the wavenumber benchmark solution (dashed lines) for a Pekeris waveguide with thickness of 100 m (physical, source and evaluation parameters given in Figure 3) along a 2.5 km path with depth $z = 46$ m. Source frequency: $f = 5$ Hz. Top panel: without attenuation ($\alpha = 0$ dB/ λ). Bottom panel: with attenuation given by $\alpha = 5$ dB/ λ .

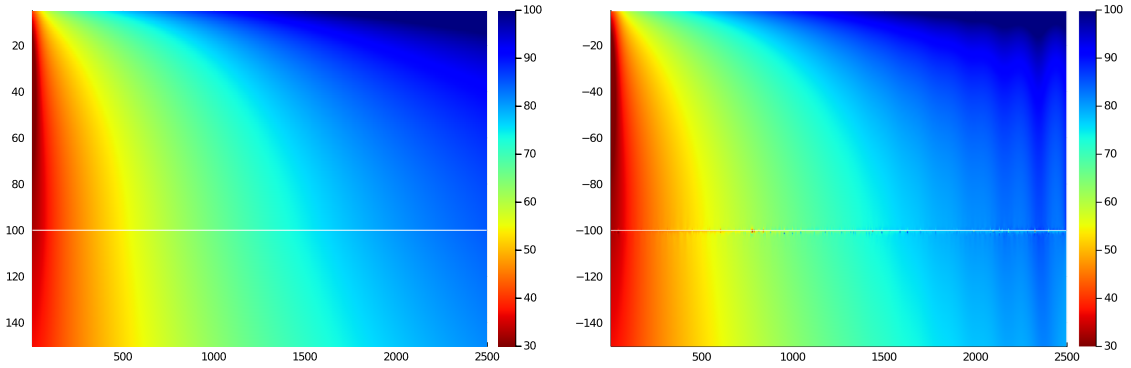


Figure 5: Transmission loss (TL) vs. range and depth, evaluated for the rectangle $0 \leq r \leq 2500$ m and $0 \leq z \leq 150$ m (without attenuation). Benchmark solution (left) and BEM solution (right) for $f = 5$ Hz. The interface water-sediments is indicated by a white line.

sediments in the cases of $\alpha = 0$ and $\alpha = 5$ dB/ λ of attenuation, respectively. A solid white line indicates the interface between both media. The left panels show the benchmark solution whereas the right ones results provided by the BEM model. In all the figures colorbars were saturated in the interval $[30, 100]$ dB for clarity purposes in the comparison. The evaluations are visually in good agreement although some numerical artifacts near the interface line, which are a consequence of the evaluation point closeness in regard the triangle' sides in the interface mesh. A finer mesh it will vanish this perturbations.

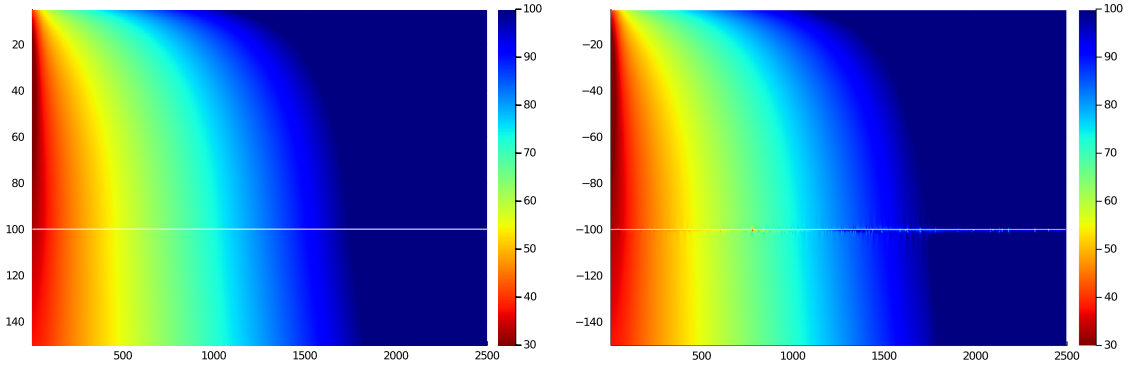


Figure 6: Transmission loss (TL) vs. range and depth evaluated for the rectangle $0 \leq r \leq 2500$ m and $0 \leq z \leq 150$ m (with attenuation given by $\alpha = 5$ dB/ λ). Benchmark solution (left) and BEM solution (right) for $f = 5$ Hz. The interface water-sediments is indicated by a white line.

3.3 Effect of the finiteness of the mesh

The propagation problem involves, as was previously mentioned, layers of almost unlimited extension. The formulation based on the half-space Green function considers the pressure-release water surface in an exact form, including also its intrinsic no-finiteness, but conversely the water-sediments interface must be discretized –taking into account the relationship between wavelength and segment length– which arises a natural question: How far should this discretization go?

The previous verifications *a priori* assumed that the region surrounding the source will be mandatory for an accurate representation of the field in the modelling, therefore the source was centred regarding the disk constituting the mesh of the bottom surface. To quantify the suitability of this centred-source assumption, we evaluate the TL corresponding to the Pekeris waveguide (at $f = 5$ Hz and $\alpha = 0$ dB/ λ) with the circular mesh of 2.5 km radius and $N = 49009$ triangles but shifting radially the source location in 625, 1250 and 2500 m. This provides four configurations which will be labelled A, B, C, D being the first them the original configuration (null shift).

The resulting TL are shown in Figure 7 where the inset in the upper right corner identifies the source location in each case. The source shift is indicated by a negative coordinate. The finite size of the mesh is clearly noticeable at each side of the curves (except in the D case) and the source location is evidenced by the sharp peak corresponding to minimum TL which is obtained at the minimum distance $(z - z_s)$ between source and evaluation point.

To quantify the error in each TL calculation, the resulting curves B, C, D are shifted to match with A . Then they are comparable point to point alongside a line of 2500 m, which is the minimum length common to all of them. Defining a relative error in the logarithmic scale according to

$$\text{Rel Err} = \frac{|\text{TL} - \text{TL}_b|}{|\text{TL}_b|} \quad (19)$$

where TL_b is the Pekeris wavenumber integration prediction (the benchmark) the relative errors associated to the different TL obtained in the four cases are shown in Figure 8. An inset in the left side shows a scheme for source location in each configuration A, B, C, D as well as the 2.5 km line segment (dashed lines) where the TL are being calculated in each case (for clarity purposes -avoiding the overlapping- in this scheme the lines are shifted a little amount in the vertical direction).

The A configuration, i.e. the source “centred” at the mesh shows the expected error of mesh-finiteness, already observed, clearly amplified towards the end of the line (beyond $r = 2500$ m there is no world!). Configurations B and C , sources shifted in 625 and 1250 m, result in a better error behaviour, because for neither one a relative error of 0.005 is surpassed. Remarkably, TL evaluation for the immediate region surrounding the source is not perturbed in these shifted cases. The extreme

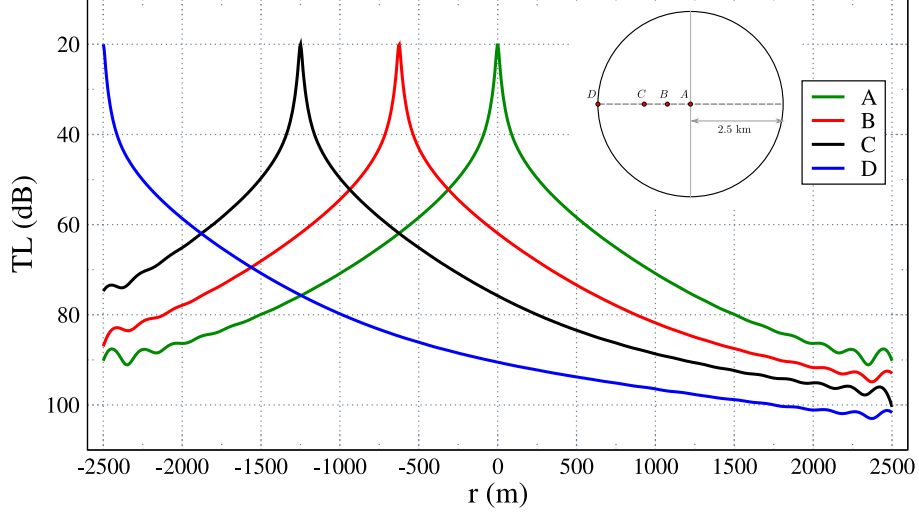


Figure 7: Transmission loss (TL) vs range computed by the BEM model for the Pekeris waveguide along a 5000 m radial path coincident with a radius of the circular mesh of $N = 49009$ triangles. The source were located at $z_s = 36$ m but shifted radially in r according to the scheme shown in the insert. The configurations A, B, C and D have the source at 0, -625, -1250 and -2500 in the coordinatization used.

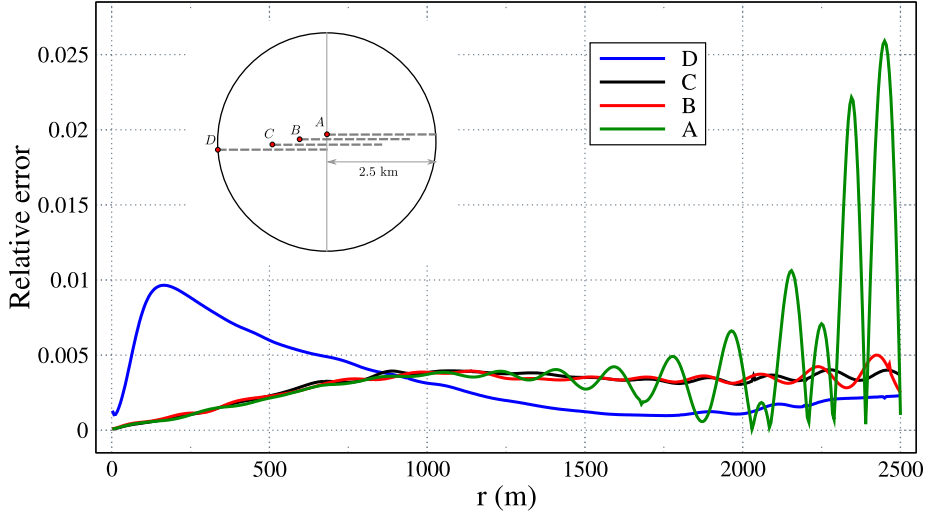


Figure 8: Relative error, according to definition (19), for the TL vs range of shifted source configurations A, B, C and D . In each case the first 2500 m from the source to the right were compared point to point with the benchmark solution. The inset in the upper left corner shows the evaluation segment compared for each case.

case of a source located in the border of the domain, configuration D , exhibits a maximum error in the first 250 m but a decreasing one afterwards.

These numerical experiments reveal that a compromise solution between accuracy and mesh use for TL calculation, along lines at least, can be attained considering a centered line of evaluation more than a centered source. The associated question which arises next is, assuming that a centered configuration as C satisfies a desired error, how to surround that segment with a mesh big enough to provide an “accurate” TL evaluation but simultaneously with little overhead due to calculation from far regions with negligible contribution. To explore this question we considered two alternative meshes build from the original circular disk; two ellipses of 2500 m major axis and minor axis in the relation 1:2 and 1:3, which results in 1250 m and 833.33 m, respectively.

The two elliptical meshes were build assuring a triangle density similar to the one used in the circular mesh. Therefore the ellipses 1:2 and 1:3 have $N = 24628$ and $N = 16285$ triangles, respectively. The relation between areas with respect to the 2500 m radius circular disk are 1/2 and 1/3 whereas the relation between the number of triangles are 0.502 and 0.332. Therefore, the triangle density is similar for all the three meshes.

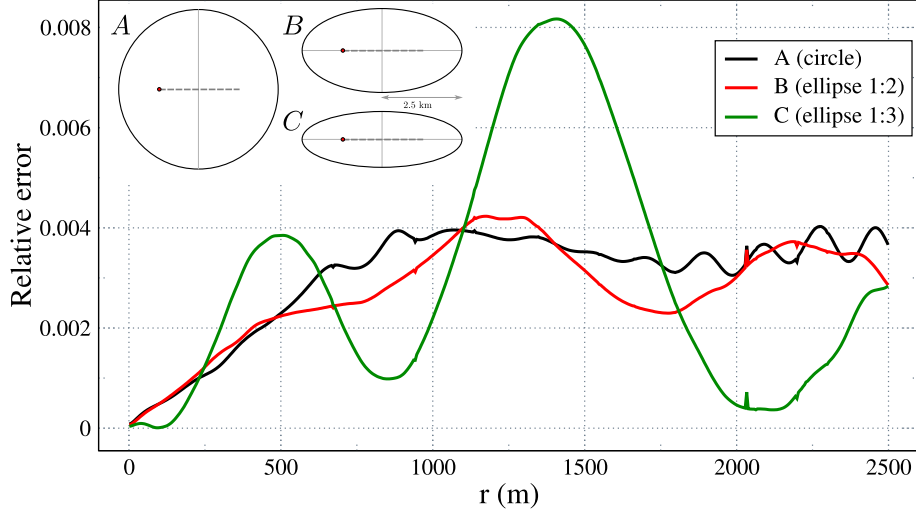


Figure 9: Relative error for TL vs range evaluated for a 2500 m segment, which is indicated by dashed lines in the scheme of the inset, for the 2500 m radius circular mesh and two elliptical meshes with major semiaxes of 2500 m and minor semiaxes in ratios 1:2 and 1:3.

In the Figure 9 the relative error for TL calculation along a 2500 m line, is shown for the three meshes considered. The inset at the upper left corner of the figure details the evaluation segment for the circular and the elliptical meshes. Surprisingly the decrease in the extension of the mesh has no appreciable effect in the TL since the relative error is similar. The 1:3 ellipse displays an oscillatory behaviour, which emerges as an artifact introduced by the artificial elliptic boundary delimiting the end of the computational domain. Elliptical meshes with an increased number of triangles and other aspect-ratio as 1:4, display similar behaviors in r . Nevertheless, for the 1:3 ellipse, these relative errors do not exceed 0.64 dB in absolute terms, a value which is acceptable in practical applications of acoustical propagation in the ocean.

4 BEM model in a shallow waters range dependent environment

To evaluate the model in a range dependent environment we have built a synthetic scenario provided with a non-trivial bathymetry consisting of a plane bottom of $D = 500$ m depth with a conical mountain with a height of 300 m inside. Similar scenarios were used, for example, in [12]. Transmission losses will be evaluated over a r, z plane of 2500×1000 m which cuts in half the mountain. A point source of unitary amplitude and frequency $f = 5$ Hz is located at $r = 0$ and $z_s = 250$ m. A mesh of circular shape with radius $R = 2500$ m containing the mountain surface will be used. The Figure 10 shows a 2D sketch of the evaluation plane with the physical parameters indicated over it (left) and a 3D view encompassing both, the plane and the water-sediments interface mesh (right).

The circular mesh has $N = 50000$ triangles. The given frequency involves acoustics wavelengths of $\lambda_0 = 300$ m and $\lambda_1 = 360$ m for the water and sediments, respectively. Considering a maximum segment length of $\lambda/5$, and taking into account the lower wavelength it leads to a triangle' sides $\ell < 60$ m. This condition was fulfilled for the 95 % of the triangles of the mesh.

For TL evaluation two attenuation coefficients were used; $\alpha = 0$ (no attenuation) and $\alpha = 20$

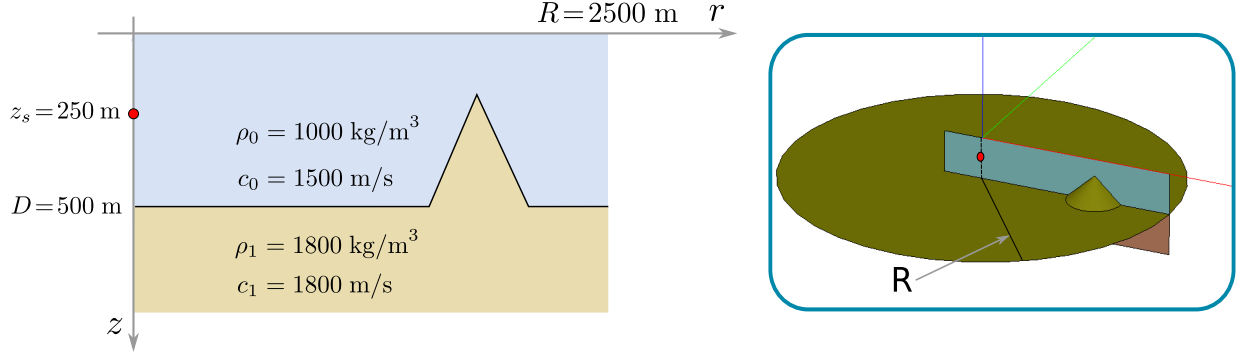


Figure 10: Scheme for a range dependent waveguide environment; a plane bottom with a depth of 500 m provided with a conical mountain with a height of 300 m. TL will be evaluated over a plane of 2500 x 1000 m in r, z which is shown with the propagation parameters overimposed (left) and in a 3D panoramic view (right).

dB/ λ , the latter a value big enough only aimed to show a remarkably different graphical result. In Figure 11 results for TL in the rz -plane are shown: the no attenuation case (left panel) and the $\alpha = 20$ dB/ λ one (right panel). The color bar values were saturated for a better contrast. The water-sediments interface is indicated by a white line showing that the TL changes continuously when the interface is crossed. The region surrounding the source shows brighter indicating low TL values, as were expected.

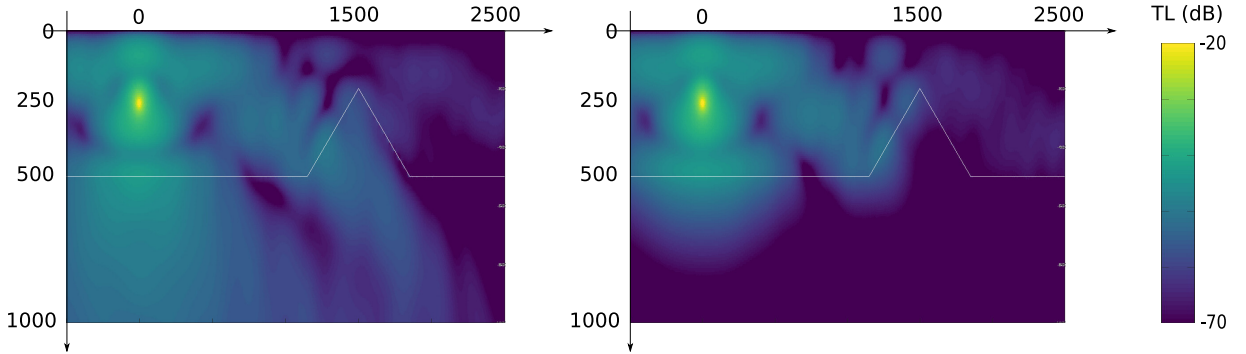


Figure 11: Transmission loss (TL) evaluated over the (r, z) -plane previously shown in the Figure 10. The white line indicates the water-sediments interface. The left panel considers attenuation $\alpha = 0$ whereas the right one $\alpha = 20$ dB/ λ . The color bar on the right is saturated for a better contrast.

The intense attenuation due to the selected α -value accounts for the fast vanishing of the pressure field and consequent increase of the transmission losses. Moreover, it is noticeable that the conical mountain presence does not preclude appreciably pressure fields behind it; which is an effect of the relative low frequency and diffraction effects due to the boundaries.

5 Conclusions

For an underwater acoustic propagation problem the BEM approach provides a clean formulation regarding the field behaviour at infinity, as a consequence of automatically fulfilling of the radiation condition. There is no need of artificial boundaries and layers, required in other methods to avoid emergence of spurious numerical artifacts. Discretization of the entire domain boundary is not required to achieve an acceptable prediction but still this “local approach” to the problem can still be computationally demanding at the frequency ranges of interest for some applications. The formulation based on a half-space Green function requires some tweaking of the integral operators

for enabling to consider an infinite pressure release surface (Dirichlet condition). An infinite acoustic hard surface (Neumann condition) suitable for modelling propagation over a rigid bottom can be worked out in the same fashion with minor modifications.

For an admissible accuracy in the TL evaluation a mesh considering a limited region near the source is enough. Even for moderated frequencies that implies very large matrix systems; thus, there is a clear need of iterative methods for the system solving stage and accelerated integral evaluations, two key components to avoid the explicit matrix construction and fast evaluation of the matrix elements, respectively.

Author Contribution and Funding

EL: algorithm implementation, theoretical development, numerical simulations, methodology, formal analysis, and writing – original draft. JDG: theoretical development, methodology, formal analysis, and writing – original draft. SB: methodology, formal analysis, and writing – review and editing. All authors contributed to the article and approved the submitted version. This work was supported by the Program of the Argentinian Ministry of Defense (PIDDEF 02/20), the Argentinian Navy and the National Council for Scientific and Technical Research (CONICET)

A Boundary integral equation from boundary conditions at Γ_1

Evaluation of an integral operator $U[\varphi]$ at a boundary point $x \in \Gamma_1$ approached from the region R_0 , is calculated as the limit

$$U[\varphi](x) = \lim_{h \rightarrow 0} U[\varphi](x + h\hat{n}),$$

where x is reached along the normal direction given by \hat{n} (the normal at x) from the point $x_0 \in R_0$ (see Figure 12). The operator evaluation at x but approached from the region R_1 proceed along the opposite direction (i.e. along $-\hat{n}$) from the point $x_1 \in R_1$, i.e.

$$U[\varphi](x) = \lim_{h \rightarrow 0} U[\varphi](x - h\hat{n}),$$

where $h > 0$ in both cases.

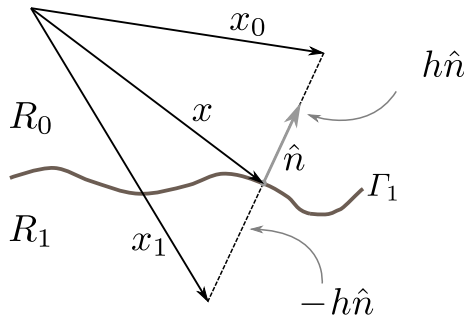


Figure 12: Sketch for normal derivative evaluation.

By inserting the prescriptions (10) in Eqs. (4) and defining $x^+ = x + h\hat{n}$ and $x^- = x - h\hat{n}$ the boundary conditions can be considered as $h \rightarrow 0$ limits,

$$\lim_{h \rightarrow 0} \rho_0 (S_0[\phi](x^+) + K_0[\psi](x^+) + \bar{u}^{\text{src}}(x^+)) = \lim_{h \rightarrow 0} \rho_1 (S_1[\phi](x^-) + K_1[\psi](x^-))$$

$$\lim_{h \rightarrow 0} K'_0[\phi](x^+) + T_0[\psi](x^+) + \partial_n \bar{u}^{\text{src}}(x^+) = \lim_{h \rightarrow 0} K'_1[\phi](x^-) + T_1[\psi](x^-)$$

where the evaluation point x^+ tends to Γ_1 from R_0 whereas point x^- tends from R_1 . Evaluating the $h \rightarrow 0$ limit and considering the jump (*jump and continuity conditions*, see theorem 3.1 of [24]) for K_i and S_i , we obtain

$$\rho_0 S_0[\phi](x) - \rho_1 S_1[\phi](x) + \rho_0 K_0[\psi](x) - \rho_1 K_1[\psi](x) + \alpha_{01} I[\psi](x) = -\rho_0 \bar{u}^{\text{src}}(x)$$

$$K'_0[\phi](x) - K'_1[\phi](x) - I[\phi](x) + T_0[\psi](x) - T_1[\psi](x) = -\partial_n \bar{u}^{\text{src}}(x)$$

where $\alpha_{01} = (\rho_0 + \rho_1)/2$ and I is the identity operator. Using Müller operator' definition, Eq. (12), and a more compact notation the boundary conditions results in

$$(\rho_0 S_0 - \rho_1 S_1)[\phi](x) + (\rho_0 K_0 - \rho_1 K_1 + \alpha_{01} I)[\psi](x) = -\rho_0 \bar{u}^{\text{src}}(x)$$

$$(K'_0 - K'_1 - I)[\phi](x) + \mathcal{M}_{01}[\psi](x) = -\partial_n \bar{u}^{\text{src}}(x).$$

Multiplying the last equation by -1, an usual convention, it results in the boundary integral system of Eq. (11).

B Operator's expressions for \bar{G}

The cartesian coordinate system associated to the problem is shown in Figure 13.

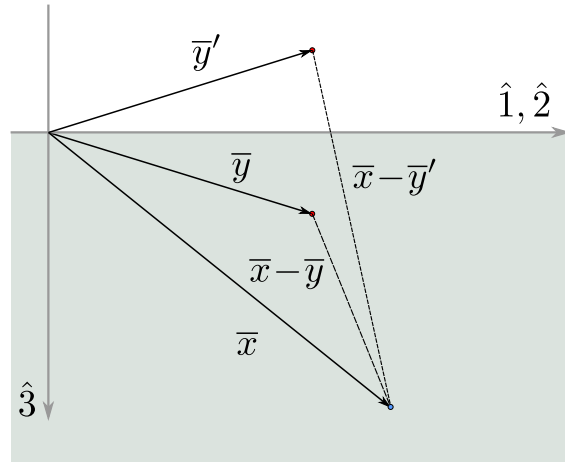


Figure 13: Coordinate system used for the graphical representation of vectors and distances involved in the half-space Green function operator's expressions.

Throughout this appendix the vector property will be explicitly emphasized by a line over the corresponding letter, for clarity reasons and to avoid confusions. With this convention the points under consideration are $\bar{x} = (x_1, x_2, x_3)$, $\bar{y} = (y_1, y_2, y_3)$ and $\bar{y}' = (y_1, y_2, -y_3)$, being useful to define

$$r = |\bar{x} - \bar{y}|, \quad r' = |\bar{x} - \bar{y}'|$$

and unitary vectors

$$\hat{r} = \frac{\bar{x} - \bar{y}}{r} = \frac{\bar{r}}{r}, \quad \hat{r}' = \frac{\bar{x} - \bar{y}'}{r'} = \frac{\bar{r}'}{r'}.$$

The half-space Green function in the wavenumber k is

$$\bar{G}(k, \bar{x}, \bar{y}) = \frac{e^{ik|\bar{x}-\bar{y}|}}{4\pi|\bar{x}-\bar{y}|} - \frac{e^{ik|\bar{x}-\bar{y}'|}}{4\pi|\bar{x}-\bar{y}'|} = \frac{e^{ikr}}{4\pi r} - \frac{e^{ikr'}}{4\pi r'} \quad (20)$$

Given that the Green function is a two-point function, it is relevant to indicate respect to what point the gradient is considered. It will be noted with a subscript in the nabla symbol; ∇_x or ∇_y .

Since the dependence of the coordinates in \bar{G} is mediated by r and r' it is convenient to use the chain rule $\nabla f(r) \equiv \partial_r f \nabla r$ and $\nabla f(r') \equiv \partial_{r'} f \nabla r'$ in the gradient calculation. By using this idea and the relations

$$\nabla_x r = \frac{\bar{r}}{r}, \quad \nabla_y r = -\frac{\bar{r}}{r}, \quad \nabla_x r' = \frac{\bar{r}'}{r'}, \quad \nabla_y r' = -\frac{1}{r'} \check{r}'$$

where \check{r}' is a vector that results from multiplying \bar{r}' by a diagonal matrix which has its third coordinate negative, i.e.

$$\check{r}' = \begin{pmatrix} 1 & 0 & 0 \\ 0 & 1 & 0 \\ 0 & 0 & -1 \end{pmatrix} \bar{r}',$$

the following useful results are obtained

$$\begin{aligned} \nabla_x \left(\frac{e^{ikr}}{4\pi r^3} \right) &= \frac{e^{ikr}}{4\pi r^3} (ikr - 1) \bar{r}, & \nabla_x \left(\frac{e^{ikr'}}{4\pi r'^3} \right) &= \frac{e^{ikr'}}{4\pi r'^3} (ikr' - 1) \bar{r}', \\ \nabla_y \left(\frac{e^{ikr}}{4\pi r^3} \right) &= -\frac{e^{ikr}}{4\pi r^3} (ikr - 1) \bar{r}, & \nabla_y \left(\frac{e^{ikr'}}{4\pi r'^3} \right) &= -\frac{e^{ikr'}}{4\pi r'^3} (ikr' - 1) \check{r}'. \end{aligned}$$

With these ingredients the kernels of the four operators are

- For $S[\varphi](x)$

$$\bar{G}(x, y) = \frac{1}{4\pi} \left[\frac{ikr}{r} - \frac{ikr'}{r'} \right]$$

- For $K[\varphi](x)$

$$\partial_{n_y} \bar{G}(x, y) = \frac{1}{4\pi} \left[\frac{ikr}{r^2} (ikr - 1) (-\hat{r} \cdot \hat{n}_y) - \frac{ikr'}{r'^2} (ikr' - 1) \left(-\frac{\check{r}'}{r'} \cdot \hat{n}_y \right) \right]$$

- For $K'[\varphi](x)$

$$\partial_{n_x} \bar{G} dS_y = \frac{1}{4\pi} \left[\frac{ikr}{r^2} (ikr - 1) (\hat{r} \cdot \hat{n}_x) - \frac{ikr'}{r'^2} (ikr' - 1) (\hat{r}' \cdot \hat{n}_x) \right]$$

- For $T[\varphi](x)$

$$\begin{aligned} \partial_{n_x} \partial_{n_y} \bar{G}_k(x, y) &= \\ &= \frac{e^{ikr}}{4\pi r^3} \left\{ [3(ikr - 1) + k^2 r^2] (\hat{r} \cdot \hat{n}_x) (\hat{r} \cdot \hat{n}_y) - (ikr - 1) \hat{n}_x \cdot \hat{n}_y \right\} + \\ &+ \frac{e^{ikr'}}{4\pi r'^3} \left\{ [3(ikr' - 1) + k^2 r'^2] (\hat{r} \cdot \hat{n}_x) \left(\frac{\check{r}'}{r'} \cdot \hat{n}_y \right) - (ikr' - 1) \partial_{n_x} (\check{r}' \cdot \hat{n}_y) \right\}, \end{aligned}$$

where the last factor in the second term of the T operator is

$$\partial_{n_x} (\check{r}' \cdot \hat{n}_y) = \hat{r}' \cdot \hat{n}_x \left(\frac{\check{r}'}{r'} \right) \cdot \hat{n}_y + \hat{n}_x \cdot \begin{pmatrix} 1 & 0 & 0 \\ 0 & 1 & 0 \\ 0 & 0 & -1 \end{pmatrix} \hat{n}_y - \hat{n}_x \cdot \left(\frac{\check{r}'}{r'} \right) \hat{r}' \cdot \hat{n}_y.$$

References

- [1] Buckingham, M. J. (1992). Ocean-acoustic propagation models. *Journal d'acoustique (Les Ulis)*, 5(3):223–287.
- [2] Tolstoy, A. (1996). 3-d propagation issues and models. *Journal of Computational Acoustics*, 4(03):243–271.
- [3] Sturm, F. and Korakas, A. (2013). Comparisons of laboratory scale measurements of three-dimensional acoustic propagation with solutions by a parabolic equation model. *The Journal of the Acoustical Society of America*, 133(1):108–118.
- [4] Oliveira, T. C., Lin, Y.-T., and Porter, M. B. (2021). Underwater sound propagation modeling in a complex shallow water environment. *Frontiers in Marine Science*, page 1464.
- [5] Lin, Y.-T., Newhall, A. E., Miller, J. H., Potty, G. R., and Vigness-Raposa, K. J. (2019). A three-dimensional underwater sound propagation model for offshore wind farm noise prediction. *The Journal of the Acoustical Society of America*, 145(5):EL335–EL340.
- [6] Heaney, K. D. and Campbell, R. L. (2016). Three-dimensional parabolic equation modeling of mesoscale eddy deflection. *The Journal of the Acoustical Society of America*, 139(2):918–926.
- [7] Taroudakis, M., Athanassoulis, G., and Ioannidis, J. (1990). A variational principle for underwater acoustic propagation in a three-dimensional ocean environment. *The Journal of the Acoustical Society of America*, 88(3):1515–1522.
- [8] Porter, M. B. (1992). The kraken normal mode program. Technical report, Naval Research Lab Washington DC.
- [9] DeCourcy, B. J. and Duda, T. F. (2020). A coupled mode model for omnidirectional three-dimensional underwater sound propagation. *The Journal of the Acoustical Society of America*, 148(1):51–62.
- [10] de Moraes Calazan, R. and Rodríguez, O. C. (2018). Simplex based three-dimensional eigenray search for underwater predictions. *The Journal of the Acoustical Society of America*, 143(4):2059–2065.
- [11] Porter, M. B. (2019). Beam tracing for two-and three-dimensional problems in ocean acoustics. *The Journal of the Acoustical Society of America*, 146(3):2016–2029.
- [12] Lin, Y.-T., Duda, T. F., and Newhall, A. E. (2013). Three-dimensional sound propagation models using the parabolic-equation approximation and the split-step fourier method. *Journal of Computational Acoustics*, 21(01):1250018.
- [13] Boyles, C. A. (1984). *Acoustic waveguides: applications to oceanic science*. John Wiley and Sons Inc.
- [14] Dawson, T. W. and Fawcett, J. A. (1990). A boundary integral equation method for acoustic scattering in a waveguide with nonplanar surfaces. *The Journal of the Acoustical Society of America*, 87(3):1110–1125.
- [15] Santiago, J. and Wrobel, L. (2004). Modified green’s functions for shallow water acoustic wave propagation. *Engineering Analysis with Boundary Elements*, 28(11):1375–1385.
- [16] Seybert, A. and Soenarko, B. (1988). Radiation and scattering of acoustic waves from bodies of arbitrary shape in a three-dimensional half space. *Journal of vibration, acoustics, stress, and reliability in design*, 110(1):112–117.

- [17] Li, C., Campbell, B. K., Liu, Y., and Yue, D. K. (2019). A fast multi-layer boundary element method for direct numerical simulation of sound propagation in shallow water environments. *Journal of Computational Physics*, 392:694–712.
- [18] Jensen, F. B., Kuperman, W. A., Porter, M. B., Schmidt, H., and Tolstoy, A. (1994). *Computational Ocean Acoustics*. American Institute of Physics.
- [19] Foote, K. G. (1980). Importance of the swimbladder in acoustic scattering by fish: a comparison of gadoid and mackerel target strengths. *The Journal of the Acoustical Society of America*, 67(6):2084–2089.
- [20] Gonzalez, J. D., Lavia, E. F., Blanc, S., Maas, M., and Madirolas, A. (2020). Boundary element method to analyze acoustic scattering from a coupled swimbladder-fish body configuration. *Journal of Sound and Vibration*, 486:115609.
- [21] Kress, R. (2001). Specific theoretical tools. In Pike, E. R. and Sabatier, P. C., editors, *Scattering, Two-Volume Set: Scattering and Inverse Scattering in Pure and Applied Science*, pages 37–51. Elsevier.
- [22] Kress, R. and Roach, G. (1978). Transmission problems for the helmholtz equation. *Journal of Mathematical Physics*, 19(6):1433–1437.
- [23] Pekeris, C. L. (1948). Theory of propagation of explosive sound in shallow water. *Geol. Soc. Am., Memoir*, 27.
- [24] Colton, D. and Kress, R. (1998). *Inverse acoustic and electromagnetic scattering theory*, volume 93. Springer-Verlag. Berlin.